coatings

Article

Quasi-Isotropy Structure and Characteristics of the Ultrasonic-Assisted WAAM High-Toughness Al Alloy

Wei Luo [1], Peng Xu [1,2,*], Ming Zhang [3] and Jiangshan Li [3]

[1] College of Materials and Metallurgy, Guizhou University, Guiyang 550025, China; 18584457072@163.com
[2] Teaching and Scientific Research Center, Guizhou Qiannan Economic College, Qiannan 550600, China
[3] HanKaiSi Intelligent Technology Co., Ltd., Guiyang 550016, China; 18121768010@163.com (M.Z.); 15772060946@163.com (J.L.)
* Correspondence: author: pxu2@gzu.edu.cn

Abstract: Wire Arc Additive Manufacturing (WAAM) has emerged as a highly promising method for the production of large-scale metallic structures; nonetheless, the presence of microstructural inhomogeneities, anisotropic properties, and porosity defects within WAAM Al alloys has substantially hindered their broader application. To surmount these obstacles, ultrasonic-assisted WAAM was applied in the fabrication of thin-wall structures utilizing 7075 Al alloy. This study investigates the effects of ultrasonic-assisted Wire Arc Additive Manufacturing (WAAM) on the structural and mechanical properties of 7075 Al alloy specimens. Microstructural analysis showed a significant refinement in grain distribution, with the average grain size notably reduced, enhancing the material's homogeneity. Porosity across the specimens was quantified, showing a decrease in values from the upper (0.02151) to the middle (0.01347) and lower sections (0.01785), correlating with the rapid cooling effects of WAAM. Mechanical testing revealed that ultrasonic application contributes to a consistent hardness pattern, with measurements averaging 70.71 $HV_{0.1}$ horizontally and 71.23 $HV_{0.1}$ vertically, and significantly impacts tensile strength; the horizontally oriented specimen exhibited a tensile strength of 236.03 MPa, a yield strength of 90.29 MPa, and an elongation of 31.10% compared to the vertically oriented specimen which showed reduced mechanical properties due to the presence of defects such as porosity and cracks. The fracture morphology analysis confirmed a predominantly ductile fracture mode, supported by the widespread distribution of dimples on the fracture surface. The integration of ultrasonic vibrations not only refined the grain structure but also modified the secondary phase distribution, enhancing the quasi-isotropic properties of the alloy. These results underline the potential of ultrasonic-assisted WAAM in improving the performance of the 7075 Al alloy for critical applications in the aerospace and automotive industries, suggesting a promising direction for future research and technological advancement in additive manufacturing processes.

Keywords: WAAM; 7075 Al; quasi-isotropic; ultrasonic-assisted

check for updates

Citation: Luo, W.; Xu, P.; Zhang, M.; Li, J. Quasi-Isotropy Structure and Characteristics of the Ultrasonic-Assisted WAAM High-Toughness Al Alloy. *Coatings* **2024**, *14*, 551. https://doi.org/10.3390/coatings14050551

Academic Editors: Ramachandran Chidambaram Seshadri and A.K. Lakshminarayanan

Received: 29 March 2024
Revised: 22 April 2024
Accepted: 24 April 2024
Published: 28 April 2024

Copyright: © 2024 by the authors. Licensee MDPI, Basel, Switzerland. This article is an open access article distributed under the terms and conditions of the Creative Commons Attribution (CC BY) license (https://creativecommons.org/licenses/by/4.0/).

1. Introduction

Al alloys from the Al-Zn-Mg-Cu system, notably the 7075 series, are extensively utilized across various sectors, including industry and construction, owing to their superior properties such as high strength, exceptional toughness, reduced density [1,2]. As the demand for fabricating large-scale structures and intricate components escalates, especially in endeavors to achieve high reliability, light weight, extended durability, and cost efficiency, the technology for producing high-strength Al alloys has experienced significant progression [3]. Wire Arc Additive Manufacturing (WAAM), a technique leveraging an arc as the heat source for melting a metal wire, which is subsequently deposited following a pre-defined trajectory to form the desired object upon cooling, stands out for its cost-effectiveness and high efficiency in manufacturing. Specifically, to fabricate components from the 7075 Al alloy with elevated efficiency and superior quality, WAAM emerges as an essential and innovative approach [4].

The quintessential objective of leveraging additive manufacturing technology is to ascertain that the components produced align with operational performance requirements. This encompasses crucial mechanical attributes such as hardness, strength, ductility, and corrosion resistance [5]. However, the 7075 Al alloy, characterized by its high strength but limited weldability, is particularly prone to cracking and porosity due to the rapid thermal cycles intrinsic to the WAAM process [6]. In their investigation of ultra-high-strength Al-Zn-Mg-Cu alloys fabricated via WAAM, Dong et al. determined that each individual deposition layer was composed of two types of columnar grains, each distinct in texture and origin. It was observed that the average yield strength and ultimate strength in the vertical direction were superior to those in the horizontal direction, while the differences in elongation were minimal [7]. To mitigate these challenges, scholars have explored diverse methodologies. Initial efforts to fine-tune WAAM (Wire Arc Additive Manufacturing) parameters yielded samples exhibiting enhanced microstructural uniformity and superior attributes. Wang et al. examined the impact of the electrode positive/negative (EP/EN) ratio on the CMT-WAAM process for Al-Zn-Mg-Cu alloys [8]. In related research, Yuan et al. enhanced grain refinement and mechanical properties in Al-Zn-Mg-Cu alloys during the WAAM process by introducing heterogeneous particles. Their findings indicated that the heterogeneous nucleation of TiN particles was the primary mechanism for grain refinement, with TiN particles located along grain boundaries aiding in the inhibition of grain growth. As a result of grain refinement, enhancements in both horizontal and vertical elongation rates were observed. Although the strategy of incorporating heterogeneous particles to improve microstructure proved effective, it faced stringent restrictions in fields with strict compositional standards for materials [9]. Siyu Zhou et al. implemented interlayer hammering within a hybrid WAAM process, achieving a periodic microstructure of coarse and fine grains [10]. Nevertheless, this technique extends the manufacturing cycle and diminishes productivity, particularly for sizable components. Ultrasonic-Assisted Wire Arc Additive Manufacturing (UA-WAAM) capitalizes on the benefits of ultrasonic vibration. By introducing high-frequency oscillations into the molten pool, ultrasonic vibration disrupts the solidification dynamics, thus alleviating crack formation [11,12]. These vibrations play a crucial role in dissolving oxide films commonly encountered during the welding of Al alloys, enhancing weld pool fusion and diminishing the likelihood of cracking [13,14]. Moreover, the application of ultrasonic energy aids in expelling gases from the molten pool, curtailing gas entrapment and porosity. The induced cavitation phenomena stir the molten pool vigorously, facilitating gas release and elevating weld quality [15,16]. Through UA-WAAM, grain refinement within the deposited material is achievable. High-frequency vibrations promote intense stirring and grain refinement, fostering a microstructure that could bolster mechanical properties such as the strength and fatigue resistance of the Al alloy [17,18]. Furthermore, ultrasonic vibrations enhance metallurgical cohesion between deposited layers and the substrate. These oscillations assist in oxide surface fragmentation, augment atomic diffusion, and encourage interlayer mixing, thereby reinforcing interfacial bond strength [19,20]. In essence, UA-WAAM is deployed in 7075 Al to confront the pressing concerns of cracking and porosity [21,22].

However, to date, no researchers have systematically studied the microstructure and properties of the 7075 aluminum alloy assisted by ultrasonic in the WAAM process. This investigation endeavored to construct thin-walled specimens of the 7075 Al alloy via UA-WAAM. It meticulously analyzed the microstructure and properties of the UA-WAAM specimens to discern the ultrasonic field's distinct influences on the porosity, microstructure, and secondary phase formation in WAAM 7075 Al samples.

2. Materials and Methods

2.1. Materials

The substrate material employed in this research comprises a T6 7075 Al alloy rolled plate, procured from Shenzhen Huiyu Metal Material Co., Ltd. (Shenzhen, China). The dimensions of the plate are specified as 10 mm in thickness, 50 mm in width, and 305 mm

in length. For the experimental procedures, the selected wire for welding was a 1.2 mm diameter 7075 Al alloy welding wire, produced by Hebei Lulinda Welding Material Co., Ltd. (Xingtai, China). Its elemental composition is shown in Table 1.

Table 1. Elemental composition of 7075 aluminum alloy substrates and wires.

Alloys	Al	Zn	Mg	Cu	Fe	Si	Cr
7075 Substrate	Bal.	5.65	2.61	1.46	0.25	0.11	0.22
7075 Wire	Bal.	5.56	2.46	1.64	0.42	0.05	0.20

2.2. Methods

In ultrasonically assisted processing, detrimental pressures are generated due to the local tensile stresses induced by the ultrasonic negative pressure phase within the liquid medium. This condition leads to a reduction in pressure intensity, causing the gas dissolved within the liquid to become supersaturated and subsequently nucleate into cavitation bubbles. The symbols used in the relevant equations are detailed and annotated as presented in the nomenclature.

The cavitation threshold is the lowest sound pressure or intensity needed to cause a cavitation effect in a molten pool. Here is the expression for the cavitation threshold of the Al alloy melt [23]:

$$P_B = P_0 - P_V + \frac{2}{3\sqrt{3}}\left[\frac{\left(\frac{2\sigma}{R_0}\right)}{P_0 - P_V + \frac{2\sigma}{R_0}}\right]^{\frac{1}{2}} \quad (1)$$

The core radius of dissolved air is assumed to be R_0 = 10 μm. The surface tension coefficient of the Al melt is 0.9 N/m, and the saturated vapor pressure is 2000 Pa. The corresponding cavitation threshold of the Al melt is 0.16 MPa [24].

The cavitation threshold reduces as the surface tension $2\sigma/R_0$ decreases. When the sound pressure in the molten pool exceeds the melt cavitation threshold, cavitation occurs, and cavitation bubbles form. The dynamic equation of a cavitation bubble subjected to ultrasonic action is written as [25]

$$R\ddot{R} + \frac{3}{2}\dot{R}^2 = 1/\rho[(P_0 + \frac{2\sigma}{R_0})(\frac{R_0}{R})^{3k} - \frac{2\sigma}{R} - 4\eta\frac{\dot{R}}{R} - P_0 + P_v + P_A \sin \omega t] \quad (2)$$

During the steady-state cavitation process, many cavitation bubbles continue forming due to ultrasonic positive and negative pressure interaction. At negative sound pressure, the free hydrogen in the melt quickly diffuses into the cavitation bubble and combines to form hydrogen. As a result, the hydrogen concentration of the molten pool decreases, and the volume of the bubbles increases, making it easier for the bubbles to float upward and escape [26,27].

The resonant frequency of the cavitation bubble in the steady-state cavitation process is described by the following equation [28]:

$$f = \frac{1}{2\pi R}\sqrt{\frac{3\gamma}{\rho}(P_0 + \frac{2\sigma}{R}) - \frac{2\sigma}{\rho R}} \quad (3)$$

The resonance radius of the cavitation bubble is 95.5 μm when we employ an ultrasonic wave with a frequency of 19.98 kHz. The following Stokes equation can be used to determine the rising velocity (v) of a cavitation bubble with radius R about the melt's viscosity coefficient [29]:

$$v = \frac{2gR^2(\rho - \rho_0)}{9\eta} \quad (4)$$

The calculated result was v = 34.7 mm/s. The thickness of the material used in this study was 10 mm. Assuming that the bubble's radius is constant, the time for the bubble to

escape from the molten pool is about 0.3 s. Cavitation bubbles will aggregate with each other in the process of generation and float and absorb part of hydrogen in the melt, which leads to an increase in bubble volume, meaning the bubble will escape faster, and the escape time will be less than 0.3 s [24]. The addition of the ultrasonic field accelerates the growth of bubbles in the melt pool, increasing the escape velocity of some of the bubbles, which in turn results in a reduction in porosity.

2.3. WAAM Process

The WAAM system is responsible for depositing the 7075 Al component, with its device schematic illustrated in Figure 1a. This system encompasses a Fronius CMT Advanced 4000R arc power supply (Shenzhen Xingzhongke Power Supply Technology Co.; Shenzhen, China) coupled with a wire feeding mechanism (Nantong Zhenkang Welding Electromechanical Co.; Nantong, China), a welding torch mounted on a KR 150R2700KUKA robot (KUKA Robotics (Shanghai) Co.; Shanghai, China), an argon gas delivery system, and a working platform. The parameters governing the WAAM process are detailed in Table 2. Additionally, an ultrasonic field is introduced via the CY3000X-Ultrasonic Controller transducer (Hangzhou Pansonic Ultrasonic Technology Co.; Hangzhou, China) (Figure 1b), with the specifications of the ultrasonic device enumerated in Table 3. The X-axis denotes the torch's travel direction, while the Z-axis indicates the deposition direction. A standard reference coordinate system was established using Rhino 3D NURBS software (V7.4).

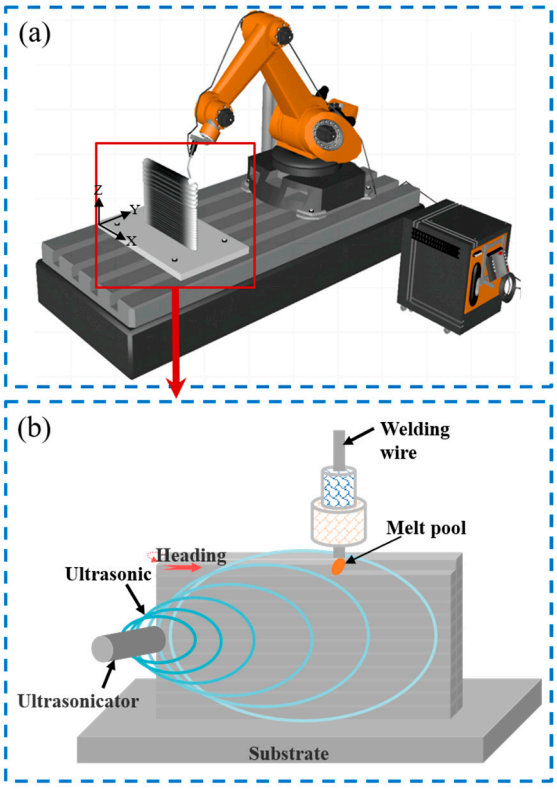

Figure 1. (**a**) Diagram illustrating the setup of the WAAM system. (**b**) Schematic diagram of the action of ultrasound on the deposited sample.

Table 2. WAAM process parameters.

Craft	Electricity	Voltage	Wire Speed	Argon Flowrate
CMT	125 A	10.4 V	7.4 m/min	20 L/min

Table 3. Parameters of the ultrasonic device.

Ultrasonic Frequency	Ultrasonic Power	Time
19.98 kHz	30%	30 min

2.4. Microstructure Study and Mechanical Properties

A wire-cutting machine using electric sparks was employed to cut 10 mm × 10 mm × 6 mm cubes in the deposition direction. The samples were polished with a polishing cloth. Electrolytic corrosion revealed the grain morphology, utilizing a 5% HF acid concentration as the etching solution. The microstructure was observed using the Olympus GX51 autobiographic optical microscope (Hangzhou Kezheng Precision Instrument Co.; Hangzhou, China) under polarized light, and the phase composition was analyzed using an X-ray diffractometer (XRD) (Sokuzumi Instruments (Shanghai) Co.; Shanghai, China). Microhardness testing was conducted using the HV-50 small-load Vickers hardness tester(Shanghai Precision Instrumentation Co.; Shanghai, China) with a loading force of 0.98 N and a 10 s holding period. Each test point was separated by 1 mm to examine the macroscopic hardness distribution across the vertical section. As illustrated in Figure 2a, tensile test samples were taken in both horizontal and vertical directions. The dimensions of the tensile specimen are shown in Figure 2b. The MTS810 microcomputer-controlled electronic universal testing machine(Suzhou Tophung Machinery Equipment Co.; Suzhou, China) was selected for tensile testing, with strain measured using a laser extensometer (elongation). The initial tension-loading velocity was set to 1 mm/min, and the tension was set to 50 N. Finally, the fractures of samples in various directions were observed using the Czech TESCAN MIRA LMS scanning electron microscope (Tyscan Trading (Shanghai) Co.; Shanghai, China).

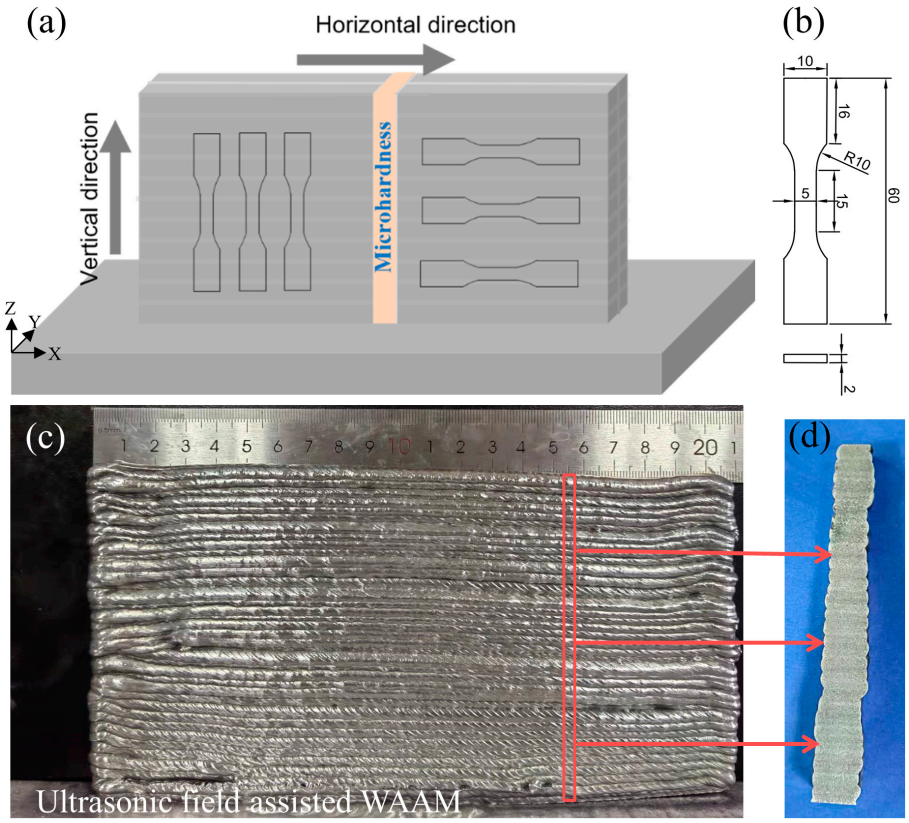

Figure 2. Schematic diagram and physical of UA-WAAM thin-wall specimen. (**a**) Sampling position. (**b**) Tensile sample dimension (mm). (**c**) The macroscopic morphology of typical walled samples. (**d**) Cross-sectional appearance.

3. Result and Discussion

3.1. Macrostructure Observation

Figure 2c displays the macroscopic texture of the deposited specimen, characterized by a repetitive pattern of concavity and convexity across the surface. This phenomenon arises from the additional ultrasonic field's influence on the weld pool's oscillatory behavior, creating an irregular overlap between successive passes. This irregularity introduces a degree of variation along the fabrication direction. Despite this, the sedimentary samples exhibit minimal macroscopic surface defects. The macroscopic attributes of the horizontal cross-section, delineated in Figure 2d, reveal distinct bright stripes, akin to findings in the research by Bai J Y et al. [30] concerning the 2219-Al alloy. These stripes signify the interlayer regions, contrasting with the intra-layer regions where pores predominantly reside.

Within the context of this study, porosity is quantified as the aggregate pore area per unit area. As delineated in Figure 3d, the porosity values for the upper, middle, and lower segments of the specimen are computed as 0.02151, 0.01347, and 0.01785, respectively. Figure 3a–c illustrate the pore distribution across the horizontal sections, highlighting a correlation with the rapid cooling associated with WAAM. Such rapid solidification confines the timeframe for bubble evacuation from the molten pool. Moreover, the dimension and positioning of these bubbles play a crucial role. The buoyancy of the bubbles, governed by their size and the interplay of buoyant and gravitational forces, dictates their movement. Consequently, smaller bubbles tend to remain near their inception point, while larger ones ascend to the melt pool's surface. This dynamic results in the formation of large air voids at the pool's upper reaches and smaller ones throughout the middle and lower sections, manifesting in a distinctive distribution pattern. The ensuing investigation will delve into the implications of these structural peculiarities on the mechanical characteristics of the 7075 Al alloy through subsequent tensile testing.

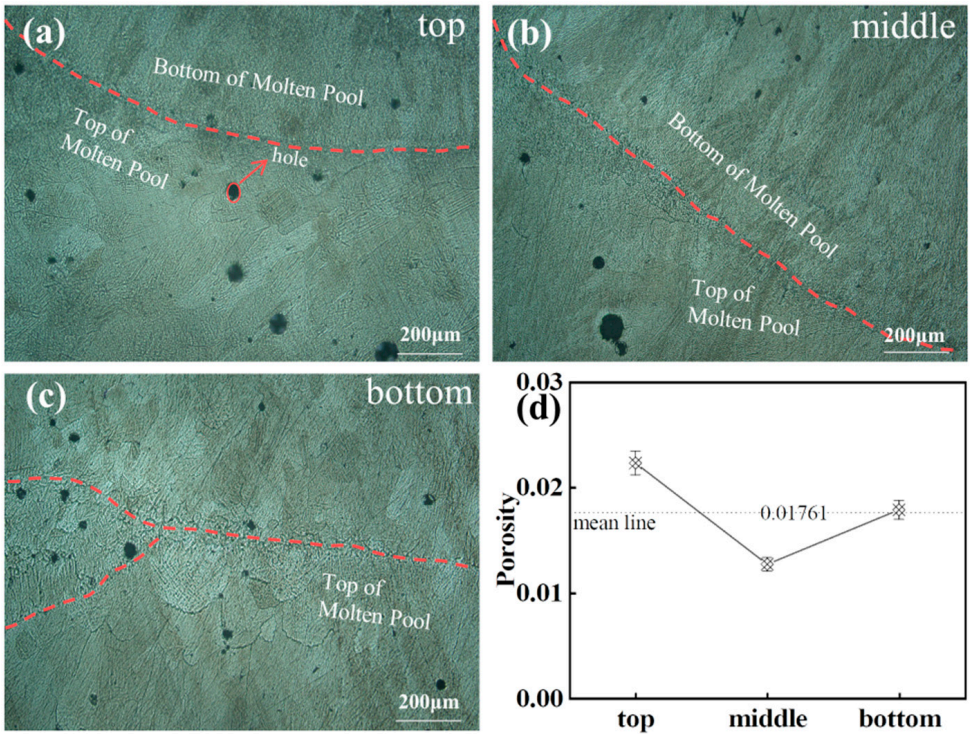

Figure 3. Pore distribution: (**a**) top, (**b**) middle, (**c**) bottom, and (**d**) porosity.

3.2. Microstructure Observation and Phase Analysis

Figure 4b–d exhibit the microstructural composition of the deposited specimens, predominantly characterized by a combination of columnar and equiaxed crystals. Upon comparison with the microstructure inherent to the conventionally processed WAAM 7075

Al alloy, it is observed that the inclusion of an ultrasonic field in the WAAM process results in a more homogenous grain distribution, with a notable reduction in grain size. This improved homogeneity and grain refinement within the molten pool's center are principally ascribed to the ultrasonic vibrations' ability to enhance molten pool fluidity and instigate dendritic fragmentation, as illustrated in Figure 4a.

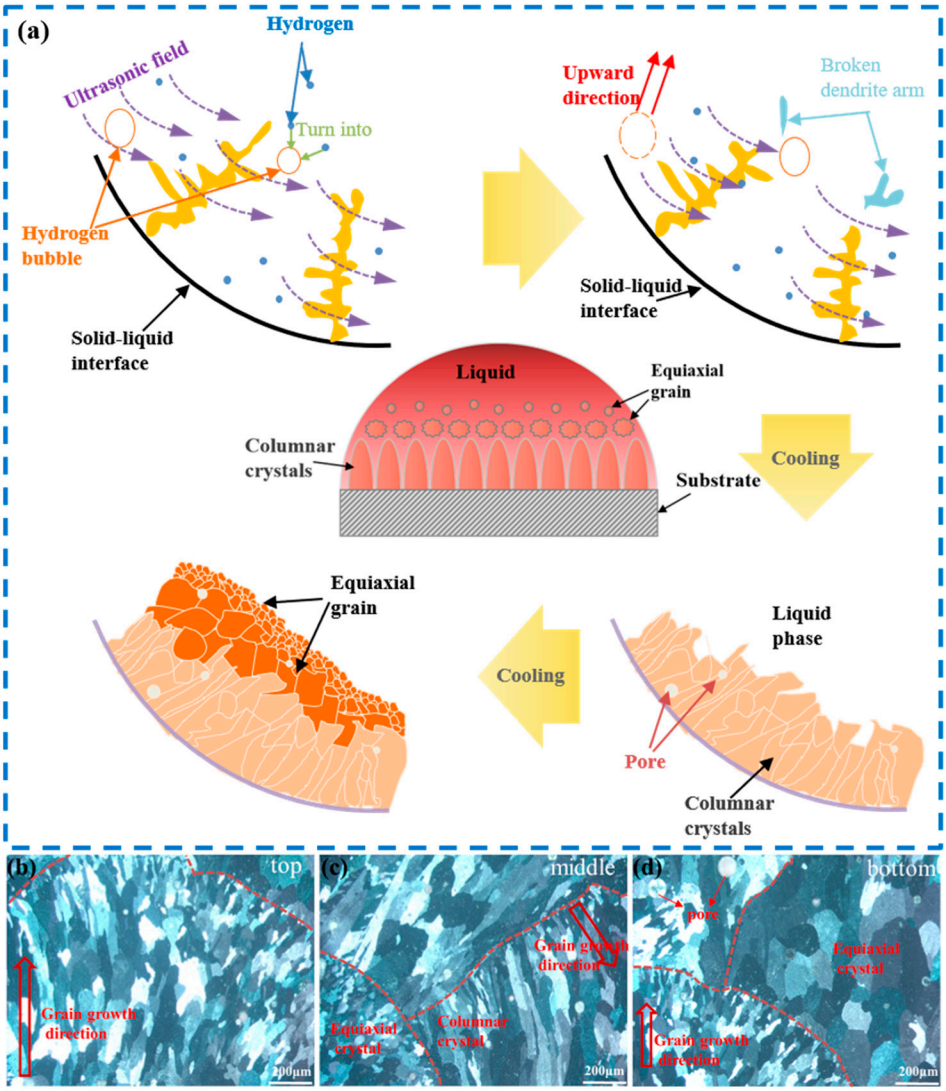

Figure 4. (**a**) Schematic diagram of organizational evolution and (**b**–**d**) multi-layer microstructure.

The precipitation in seven-series Al alloys follows the sequence of solid solution → GPI zones → metastable η′ → stable η, which is a commonly observed phase sequence. After T6 treatment, the primary enhanced precipitates consist of sub-stabilized η′, semi-co-gridded with the Al matrix. As illustrated in Figure 5, the matrix phase of the 7075 Al alloy comprises α-Al, while the primary reinforcing phase comprises $MgZn_2$. With their low content, other reinforcing phases do not show prominent diffraction peaks in XRD analysis.

The influence of the ultrasonic field on secondary phase composition cannot be exclusively discerned from X-ray Diffraction (XRD) outcomes. Consequently, an in-depth analysis concerning the effect of the ultrasonic field on the WAAM process necessitated the utilization of Energy-Dispersive Spectroscopy (EDS). Through this approach, it was determined that the secondary phase, $MgZn_2$, is uniformly distributed, a phenomenon clearly illustrated in the EDS mappings. The use of high current in the WAAM process facilitates the vaporization of the Zinc (Zn) element within the 7075 Al alloy wire during

its melting phase. This results in a diminished Zn content, and, consequently, a reduced presence of $MgZn_2$ precipitates, as evidenced in Figure 6.

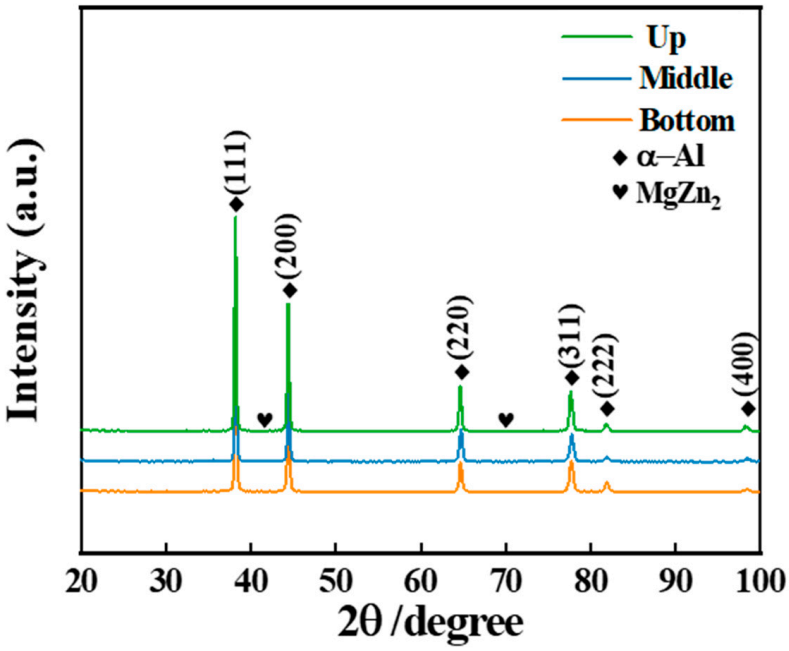

Figure 5. XRD results at different locations.

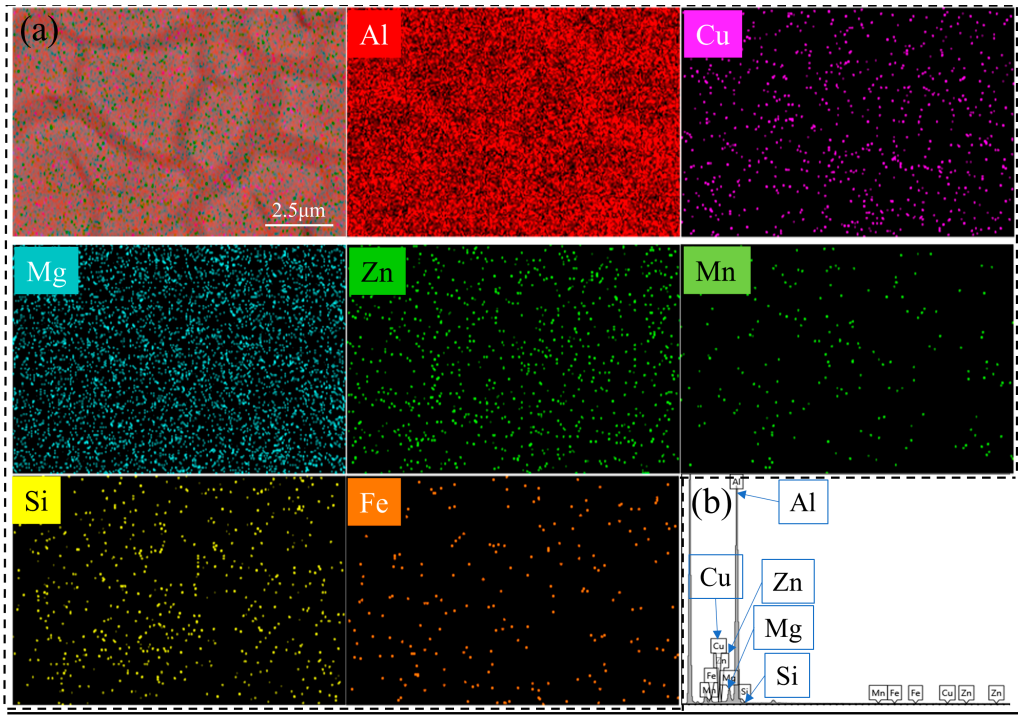

elemental	Al	Mg	Zn	Cu	Si	Fe	Mn	total
Wt%	93.84	4.28	0.90	0.06	0.47	0.25	0.20	100

Figure 6. (**a**) EDS element distribution diagram of 7075 sedimentation sample. (**b**) EDS spectrum analysis.

The application of the ultrasonic field to the WAAM process has elicited transformative effects on the microstructure and certain secondary phase formations. The ultrasonic vibrations disrupt the elongated, rod-like morphology of the $Al_6(Fe, Mn)$ secondary

phase, resulting in the emergence of irregularly shaped block structures, as illustrated in Figure 7. This alteration is anticipated to engender more uniform properties across different orientations of the deposited samples, thereby promoting isotropic characteristics in WAAM-fabricated specimens. Notably, these irregular blocks are identified as the principal nucleation sites for Iron (Fe) and Manganese (Mn), suggesting a significant role in the microstructural evolution and subsequent mechanical properties of the alloy.

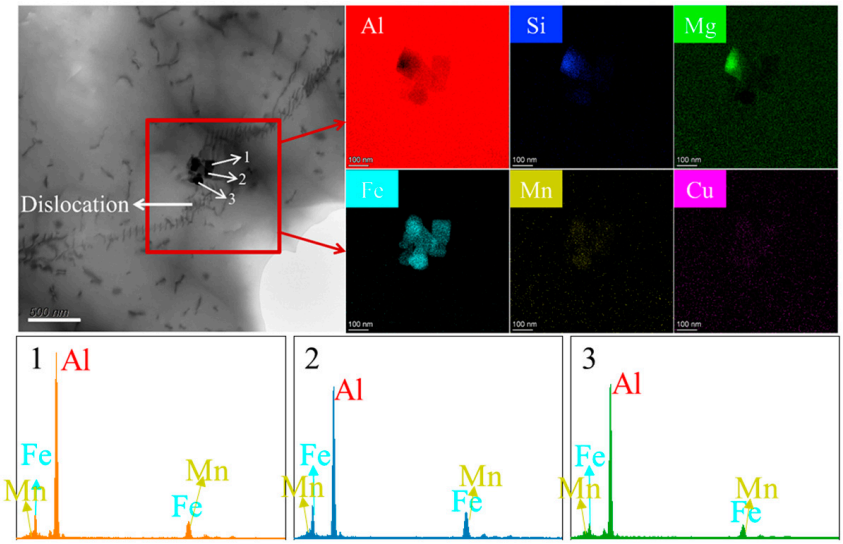

Figure 7. SEM and EDS of the Al_6(Fe, Mn) phase.

Furthermore, the presence of the Mg_2Si phase was discerned, corroborated by the findings presented in Figure 8. This observation is consistent with the research conducted by Xu et al. on the enhanced solution treatment of as-rolled Al-Zn-Mg-Cu alloys [31]. The secondary phase, comprising Mg and Si elements depicted in Figure 8, was conclusively identified as Mg_2Si through Transmission Electron Microscopy (TEM) analysis, as depicted in Figure 9. These modifications in both the microstructural and secondary phase components are instrumental in endowing the samples with quasi-isotropic properties, underscoring the ultrasonic field's pivotal role in refining the material's structural and mechanical attributes.

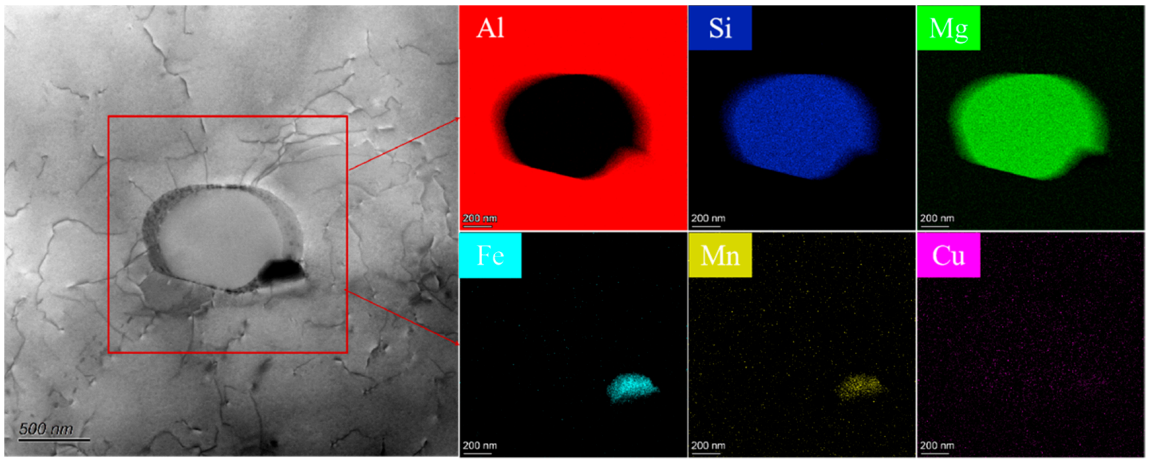

Figure 8. SEM and EDS of the Mg_2Si phase.

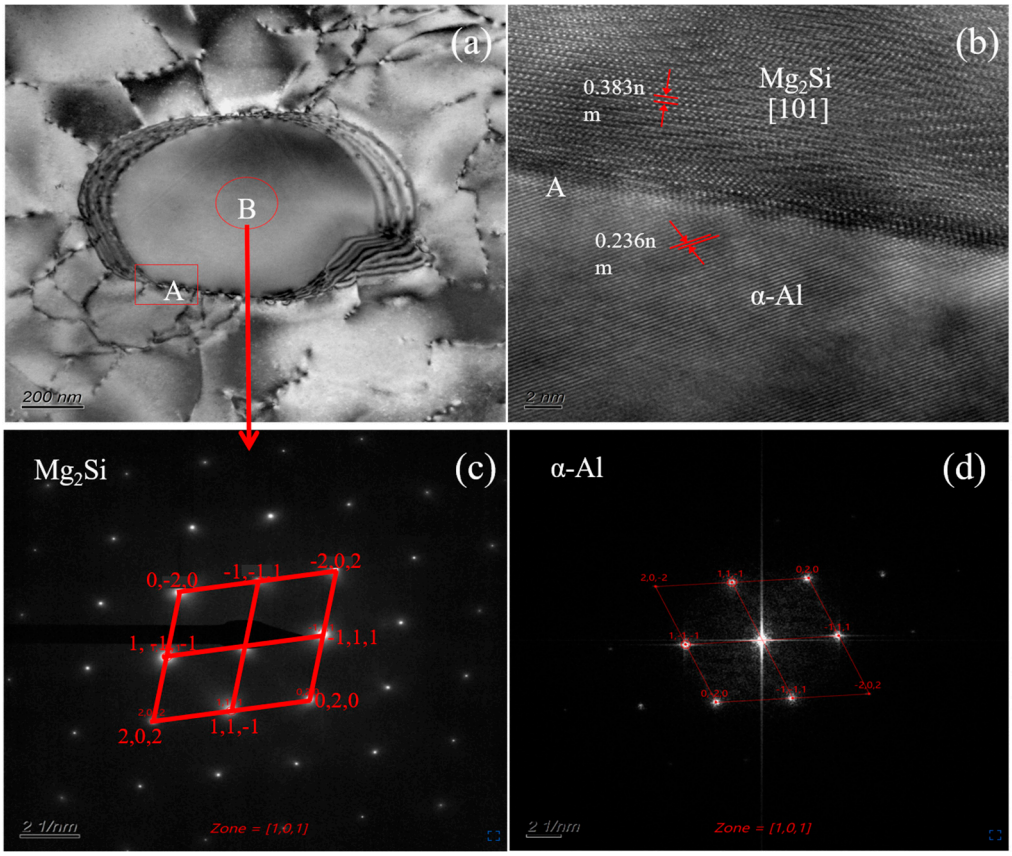

Figure 9. TEM of the Mg_2Si phase (**a**–**d**).

3.3. Mechanical Properties

Figure 10 presents the distribution of microhardness both horizontally and vertically within the deposited samples, revealing that the average hardness measures 70.71 $HV_{0.1}$ in the horizontal orientation and 71.23 $HV_{0.1}$ vertically. These hardness measurements demonstrate a uniform and consistent pattern throughout, with negligible variations between the inner and interlayer regions. This consistency in hardness distribution corroborates the Hall–Petch relationship, which posits that the value of microhardness diminishes concomitantly with an increase in grain size [32].

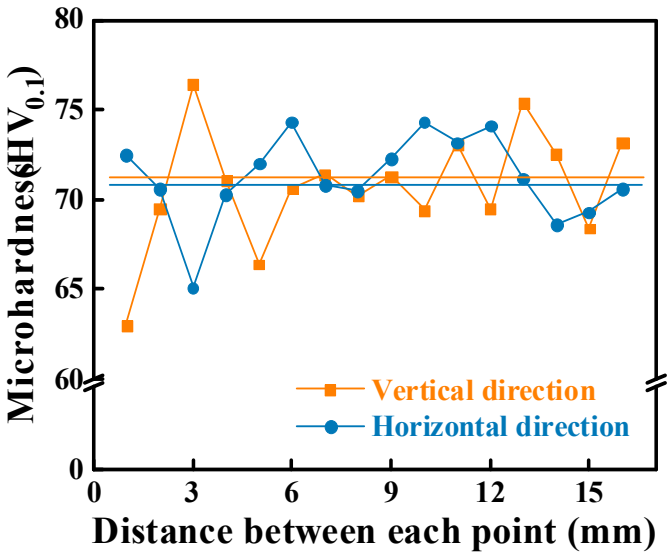

Figure 10. Micro-hardness in different directions.

Figure 11a delineates the tensile behavior of the specimen, with Figure 11b detailing the resultant tensile strength, yield strength, and elongation metrics. The specimen oriented horizontally demonstrated a tensile strength of 236.03 MPa, a yield strength of 90.29 MPa, and an elongation of 31.10%. Conversely, the specimen with vertical orientation exhibited a tensile strength of 222.85 MPa, a yield strength of 87.48 MPa, and an elongation of 22.82%. The diminished mechanical properties in the vertically oriented specimens can be ascribed to the accumulation of defects such as porosity and cracks within the interlayer regions. The primary mechanisms that enhance the strength of the 7075 Al alloy include solid solution strengthening and age hardening, endowing the 7075 Al alloy with superior strength, hardness, and corrosion resistance. The observed reduction in mechanical properties within the WAAM samples, devoid of age-hardening effects due to the absence of artificial aging, is coupled with insufficient solid solution strengthening, which is attributed to non-uniform grain distribution and the existence of secondary phase entities. Moreover, the vulnerability of WAAM samples to necking under tensile stress, leading to decreased plasticity and toughness, is principally due to a small grain size. The application of ultrasonic vibrations disrupts dendritic directional growth and refines the grains, fostering a more homogeneous structure across various orientations. Such structural refinement and modification in the secondary phase contribute to rendering the properties, like tensile strength, microhardness, and yield strength, quasi-isotropic across different dimensions of the deposited samples.

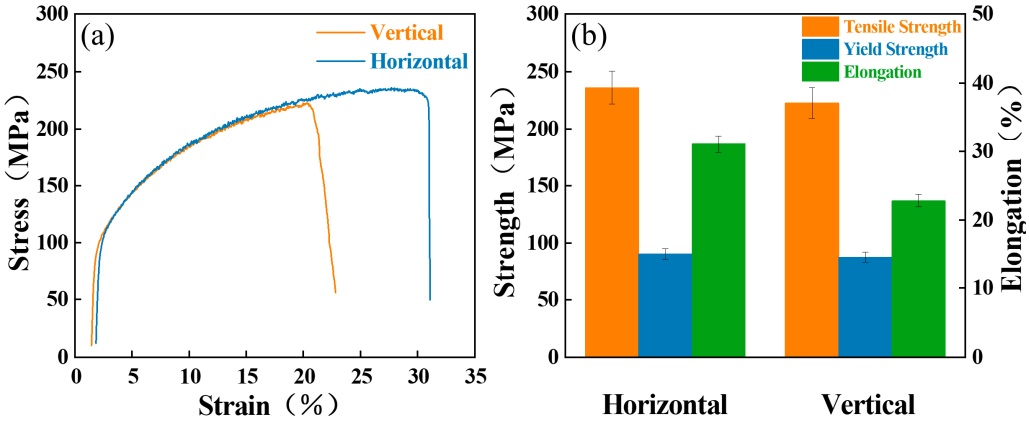

Figure 11. (**a**) Stress–strain in different directions. (**b**) Strength and elongation in different directions.

Figure 12 illustrates the fracture morphology of the tensile-tested specimen, highlighting a scant presence of voids primarily caused by element evaporation under the elevated arc temperatures characteristic of the WAAM process. Previous studies have documented that such vaporization leads to the formation of voids as the liquid Al solidifies. The sample's fracture surface showcases significant ductility, evidenced by the widespread distribution of dimples across both the horizontal and vertical directions of the fracture. The genesis of crack formation is linked to the presence of secondary phases and pores within the deposited specimen, as detailed in Figure 12a. Figure 12b reveals a morphological shift in the dimples from equiaxed to elongated forms towards the shear lip, suggesting fracture progression under shear stress. In the smoother areas depicted in Figure 12b, fish-scale dimples coalesce with traits indicative of pure shear fractures, with the red arrow signifying a parallel displacement typical of slip surface separation on the free surface. Figure 12c highlights the occurrence of equiaxed dimples within the central fracture area. This comprehensive analysis of fracture morphology unequivocally confirms that the ultrasonically assisted WAAM (UA-WAAM) Al alloy predominantly undergoes a ductile fracture mode.

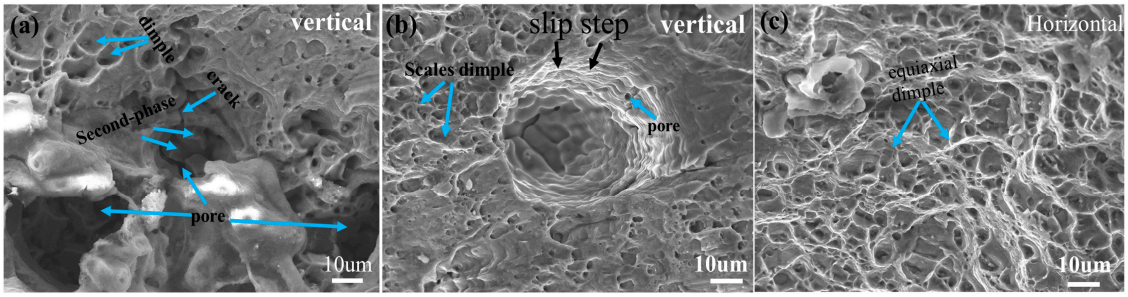

Figure 12. SEM microstructure of specimen fracture: (**a**,**b**) vertical tensile specimens; (**c**) horizontal tensile specimens.

3.4. Discussion

The macrostructural examination of the 7075 Al alloy specimens fabricated using Wire Arc Additive Manufacturing (WAAM) with ultrasonic assistance reveals a distinctive texture marked by patterns of concavity and convexity (Figure 2c). This morphology, shaped by the ultrasonic field's influence on the weld pool's dynamics, suggests enhanced surface integrity despite the observed variation along the fabrication direction. The observed bright stripes in the horizontal cross-sections (Figure 2d), similar to those reported by Bai J Y et al. [30] in the 2219-Al alloy, delineate the interlayer regions, offering insights into the layered nature of the build and its implications on structural homogeneity. Porosity remains a critical concern in WAAM processes, with this study quantifying porosity in different sections of the specimen (Figure 3d). The distribution and size of pores, influenced by the rapid cooling and the ultrasonic field, suggest a nuanced interplay between the manufacturing process and material properties, as smaller bubbles are trapped due to rapid solidification while larger bubbles migrate upwards (Figure 3a–c). This distribution impacts mechanical properties and highlights areas for optimization in controlling porosity during fabrication. The microstructural analysis further supports the beneficial impact of ultrasonic energy in WAAM. The ultrasonic field contributes to a more uniform grain distribution and reduces grain size (Figure 4b–d), enhancing the overall homogeneity of the material. Such microstructural refinement is pivotal for improving mechanical properties, as evidenced by the alteration in the morphology of the secondary phases like Al_6(Fe, Mn) and the uniform distribution of the $MgZn_2$ phase (Figures 6 and 7). The identification of the Mg_2Si phase (Figure 8) further complements the alloy's comprehensive characterization, corroborating findings from other studies like those by Xu et al. [31]. The mechanical testing results provide a robust validation of the structural observations. The hardness measurements across different orientations (Figure 10) and the tensile testing outcomes (Figure 11a,b) manifest the practical implications of microstructural enhancements brought about by the ultrasonic treatment. The uniform hardness profiles and improved tensile strength in horizontally oriented specimens suggest an effective mitigation of anisotropy, which is a common issue in additive manufacturing. The fracture morphology analysis (Figure 12) sheds light on the ductility of the material, where the predominance of ductile fracture modes, characterized by dimple formations, suggests good toughness despite the high-energy conditions of the WAAM process. The evolution of fracture characteristics under load, from equiaxed to elongated dimple forms, provides crucial insights into the material's behavior under stress and highlights the impact of secondary phases and porosity on fracture mechanisms.

The findings from this study underline the substantial influence of ultrasonic energy in refining the macrostructure, microstructure, and mechanical properties of the WAAM-fabricated 7075 Al alloy. The consistency in material properties across different sections and orientations demonstrates the potential of ultrasonic-assisted WAAM in producing high-integrity components for aerospace and automotive applications, where material performance is critical.

4. Conclusions

This research has thoroughly investigated the effects of incorporating an ultrasonic field to assist the Wire Arc Additive Manufacturing (WAAM) process for the 7075 Al alloy, demonstrating significant enhancements in the macrostructure, microstructure, and mechanical properties. The application of ultrasonic energy has led to a macroscopic pattern of concavity and convexity with minimal defects and distinctive bright stripes marking interlayer regions. Microstructurally, the introduction of ultrasonic vibrations has achieved a more homogeneous grain distribution and notable grain refinement, attributed to improved molten pool fluidity and dendritic fragmentation. This refinement plays a crucial role in the enhanced mechanical properties observed, including consistent hardness distribution and superior tensile strength in horizontally oriented specimens, which align with the Hall–Petch relationship. The ultrasonically induced modifications in the secondary phases have been instrumental in developing a quasi-isotropic nature in the material's properties. The mechanical testing results confirm that the ultrasonic-assisted WAAM process not only maintains high tensile strength and microhardness but also ensures substantial ductility, as evidenced by the fracture morphology characterized by dimple formations indicating ductile fracture modes. These findings highlight the potential of ultrasonic assistance to mitigate common defects, such as the porosity and cracks often encountered in WAAM processes, as well as explore the role of the ultrasonic field in the second phase, thereby enhancing the structural integrity and performance of the fabricated specimens. We believe that further research into the optimization of ultrasonic parameters, such as frequency and amplitude, to maximize their beneficial effects on material properties during the WAAM process is needed. Future research should also consider the economic and environmental impacts of implementing ultrasonic technology in industrial-scale manufacturing, providing a holistic view of its feasibility and sustainability.

Author Contributions: Resources, J.L.; Writing—original draft, W.L.; Funding acquisition, P.X. and M.Z. All authors have read and agreed to the published version of the manuscript.

Funding: This work was supported by the Guizhou Provincial Program on Commercialization of Scientific and Technological Achievements (QKHCG [2023] general 083).

Institutional Review Board Statement: Not applicable.

Informed Consent Statement: Not applicable.

Data Availability Statement: Data are contained within the article.

Conflicts of Interest: Ming Zhang and Jiangshan Li were employed by the company HanKaiSi Intelligent Technology Co., Ltd. The remaining authors declare that the research was conducted in the absence of any commercial or financial relationships that could be construed as a potential conflict of interest.

Nomenclature

Sign	Symbol-specific description	Sign	Symbol-specific description
R_0	cavitation core radius	K	constant
Σ	melt surface tension coefficient	R	cavitation bubble radius
P_0	standard atmospheric pressure (0.1013 MPa)	ω	angular frequency
P_v	saturated vapor pressure	f	ultrasonic frequency
$\ddot{R}$	acceleration of a point on the cavitation bubble	Γ	specific heat ratio of the gas
a	ultrasonic vibration amplitude	ρ_0	cavitation bubble gas density
η	melt viscosity coefficient (1.4×10^{-3} Pa·s)	ρ	melt density
P_A	sound pressure	η	melt viscosity coefficient

References

1. Sistiaga, M.M.; Mertens, R.; Vrancken, B.; Wang, X.; Hooreweder, B.V.; Kruth, J.P.; Humbeeck, J.V. Changing the alloy composition of Al7075 for better processability by selective laser melting. *J. Mater. Process. Technol.* **2016**, *238*, 437–445. [CrossRef]

2. Pu, B.; Lin, X.; Li, B.; Chen, X.; He, C.; Zhao, N. Effect of SiC nanoparticles on the precipitation behavior and mechanical properties of 7075Al alloy. *J. Mater. Sci.* **2020**, *55*, 6145–6160. [CrossRef]
3. Su, C.; Chen, X.; Gao, C.; Wang, Y. Effect of heat input on microstructure and mechanical properties of Al-Mg alloys fabricated by WAAM. *Appl. Surf. Sci.* **2019**, *486*, 431–440. [CrossRef]
4. Veiga, F.; Suárez, A.; Aldalur, E.; Bhujangrao, T. Effect of the Metal Transfer Mode on the Symmetry of Bead Geometry in WAAM Aluminum. *Symmetry* **2021**, *13*, 1245. [CrossRef]
5. Zhu, L.; Luo, Y.; Han, J.; Zhang, C.; Xu, J.; Chen, D. Energy characteristics of droplet transfer in wire-arc additive manufacturing based on the analysis of arc signals. *Measurement* **2019**, *134*, 804–813. [CrossRef]
6. Hu, Z.; Xu, P.; Pang, C.; Liu, Q.; Li, S.; Li, J. Microstructure and Mechanical Properties of a High-Ductility Al-Zn-Mg-Cu Aluminum Alloy Fabricated by Wire and Arc Additive Manufacturing. *J. Mater. Eng. Perform.* **2022**, *31*, 6459–6472. [CrossRef]
7. Dong, B.; Cai, X.; Lin, S.; Li, X.; Fan, C.; Yang, C.; Sun, H. Wire arc additive manufacturing of Al-Zn-Mg-Cu alloy: Microstructures and mechanical properties. *Addit. Manuf.* **2020**, *36*, 101447. [CrossRef]
8. Wang, Y.; Chen, J.; Chen, M.; Su, H.; Zhang, W.; Wu, C. Process stability and forming accuracy on wire arc additive manufactured Al–Zn–Mg–Cu alloy with different electrode positive/electrode negative ratios of CMT advance process. *Sci. Technol. Weld. Join.* **2023**, *28*, 352–361. [CrossRef]
9. Yuan, T.; Ren, X.; Chen, S.; Jiang, X. Grain refinement and property improvements of Al–Zn–Mg–Cu alloy by heterogeneous particle addition during wire and arc additive manufacturing. *J. Mater. Res. Technol.* **2022**, *16*, 824–839. [CrossRef]
10. Zhou, S.; Wang, J.; Yang, G.; Wu, B.; Xie, H.; Wu, K.; Da, A. Periodic microstructure of Al–Mg alloy fabricated by inter-layer hammering hybrid wire arc additive manufacturing: Formation mechanism, microstructural and mechanical characterization. *Mater. Sci. Eng. A* **2022**, *860*, 144314. [CrossRef]
11. Kumar, S.; Wu, C.; Padhy, G.; Ding, W. Application of ultrasonic vibrations in welding and metal processing: A status review. *J. Manuf. Process.* **2017**, *26*, 295–322. [CrossRef]
12. Abramov, O.V. *High-Intensity Ultrasonics: Theory and Industrial Applications*; CRC Press: Leiden, The Netherlands, 1999.
13. Ji, F.; Hu, Z.; Qin, X.; Ni, M.; Xiong, X.; Liu, G. Improving microstructure and mechanical properties of thin-wall part fabricated by wire arc additive manufacturing assisted with high-intensity ultrasound. *J. Mater. Sci.* **2023**, *58*, 2381–2395. [CrossRef]
14. Ji, F.; Hu, Z.; Qin, X.; Yin, F.; Ni, M.; Xiong, X. Grain refinement and mechanism of steel in ultrasound assisted wire and arc additive manufacturing. *Int. Commun. Heat Mass Transf.* **2023**, *143*, 106724. [CrossRef]
15. Teyeb, A.; Silva, J.; Kanfoud, J.; Carr, P.; Gan, T.-H.; Balachandran, W. Improvements in the Microstructure and Mechanical Properties of Aluminium Alloys Using Ultrasonic-Assisted Laser Welding. *Metals* **2022**, *12*, 1041. [CrossRef]
16. Xu, H.; Jian, X.; Meek, T.T.; Han, Q. Degassing of molten aluminium A356 alloy using ultrasonic vibration. *Mater. Lett.* **2004**, *58*, 3669–3673. [CrossRef]
17. Lyu, F.; Hu, K.; Wang, L.; Gao, Z.; Zhan, X. Regionalization of microstructure characteristics and mechanisms of slip transmission in oriented grains deposited by wire arc additive manufacturing. *Mater. Sci. Eng. A* **2022**, *850*, 143529. [CrossRef]
18. Shi, L.; Wu, C.; Liu, X. Modeling the effects of ultrasonic vibration on friction stir welding. *J. Mater. Process. Technol.* **2015**, *222*, 91–102. [CrossRef]
19. Herzog, D.; Seyda, V.; Wycisk, E.; Emmelmann, C. Additive manufacturing of metals. *Acta Mater.* **2016**, *117*, 371–392. [CrossRef]
20. Zhang, J.; Xing, Y.; Zhang, J.; Cao, J.; Yang, F.; Zhang, X. Effects of In-Process Ultrasonic Vibration on Weld Formation and Grain Size of Wire and Arc Additive Manufactured Parts. *Materials* **2022**, *15*, 5168. [CrossRef]
21. Wang, T.; Mazánová, V.; Liu, X. Ultrasonic effects on gas tungsten arc based wire additive manufacturing of aluminum matrix nanocomposite. *Mater. Des.* **2022**, *214*, 110393. [CrossRef]
22. Rostamiyan, Y.; Seidanloo, A.; Sohrabpoor, H.; Teimouri, R. Experimental studies on ultrasonically assisted friction stir spot welding of AA6061. *Arch. Civ. Mech. Eng.* **2015**, *15*, 335–346. [CrossRef]
23. Kang, J.; Zhang, X.; Wang, S.; Ma, J.; Huang, T. The comparison of ultrasonic effects in different metal melts. *Ultrasonics* **2015**, *57*, 11–17. [CrossRef] [PubMed]
24. Liu, J.; Zhu, H.; Li, Z.; Cui, W.; Shi, Y. Effect of ultrasonic power on porosity, microstructure, mechanical properties of the aluminium alloy joint by ultrasonic assisted laser-MIG hybrid welding. *Opt. Laser Technol.* **2019**, *119*, 105619. [CrossRef]
25. Nagasivamuni, B.; Ravi, K.R. Discussions on the Mechanism of Grain Refinement in Ultrasonic Treated Ti Containing Mg–Al Alloys. *Trans. Indian Inst. Met.* **2015**, *68*, 1161–1165. [CrossRef]
26. Zhang, L.; Li, X.Q.; Li, R.Q.; Jiang, R.P.; Zhang, L.H. Effects of high-intensity ultrasound on the microstructures and mechanical properties of ultra-large 2219 Al alloy ingot. *Mater. Sci. Eng. A—Struct. Mater. Prop. Microstruct. Process.* **2019**, *763*, 10. [CrossRef]
27. Feng, H.K.; Yu, S.R.; Li, Y.L.; Gong, L.Y. Effect of ultrasonic treatment on microstructures of hypereutectic Al–Si alloy. *J. Mater. Process. Technol.* **2008**, *208*, 330–335. [CrossRef]
28. Phillips, D.; Chen, X.; Baggs, R.; Rubens, D.; Violante, M.; Parker, K.J. Acoustic backscatter properties of the particle/bubble ultrasound contrast agent. *Ultrasonics* **1998**, *36*, 883–892. [CrossRef] [PubMed]
29. Hua, C.; Lu, H.; Yu, C.; Chen, J.-M.; Wei, X.; Xu, J.-J. Reduction of ductility-dip cracking susceptibility by ultrasonic-assisted GTAW. *J. Mater. Process. Technol.* **2017**, *239*, 240–250. [CrossRef]
30. Bai, J.; Fan, C.; Lin, S.B.; Yang, C.; Dong, B. Effects of thermal cycles on microstructure evolution of 2219-Al during GTA-additive manufacturing. *Int. J. Adv. Manuf. Technol.* **2016**, *87*, 2615–2623. [CrossRef]

31. Xu, D.; Rometsch, K.P.A.; Birbilis, N. Improved solution treatment for an as-rolled Al–Zn–Mg–Cu alloy. Part I. Characterisation of constituent particles and overheating. *Mater. Sci. Eng. A* **2012**, *534*, 234–243. [CrossRef]
32. Loucif, A.; Figueiredo, R.B.; Baudin, T.; Brisset, F.; Chemam, R.; Langdon, T.G. Ultrafine grains and the Hall–Petch relationship in an Al–Mg–Si alloy processed by high-pressure torsion. *Mater. Sci. Eng. A* **2012**, *532*, 139–145. [CrossRef]

Disclaimer/Publisher's Note: The statements, opinions and data contained in all publications are solely those of the individual author(s) and contributor(s) and not of MDPI and/or the editor(s). MDPI and/or the editor(s) disclaim responsibility for any injury to people or property resulting from any ideas, methods, instructions or products referred to in the content.